BNL-79961-2008-IR
CONFORM-EMMA-ACC-RPT-0001-V1.0-JSBERG-LATTICE

The EMMA Main Ring Lattice

J. Scott Berg

March 2008

Physics Department/Bldg. 901A

Brookhaven National Laboratory
P.O. Box 5000
Upton, NY 11973-5000
www.bnl.gov

DISCLAIMER

The EMMA Main Ring Lattice

J. Scott Berg [1]

Brookhaven National Laboratory; Building 901A; P.O. Box 5000; Upton, NY 11973-5000

Abstract

I give a brief introduction to the purpose and goals of the EMMA experiment and describe how they will impact the design of the main EMMA ring. I then describe the mathematical model that is used to describe the EMMA lattice. Finally, I show how the different lattice configurations were obtained and list their parameters.

Key words: linear non-scaling fixed field alternating gradient accelerator
PACS: 29.20.D-, 29.27.Bd, 41.85.-p

1. Goals of the Experiment and Lattice

The purpose of the EMMA experiment is to provide a platform for the study of a linear non-scaling FFAG. Such a machine has been contemplated for a number of applications: muon acceleration for a neutrino factory or muon collider [1–4], high-power proton drivers [5,6], medical accelerators [7–9,6,10], and other applications [11,12]. The most extensive studied of these applications is the muon acceleration application, and was therefore used as a basis for the design of the EMMA main ring. This application requires that the acceleration be very rapid (under 20 turns in most cases), and uses RF with a constant frequency. The particles are highly relativistic, and the lattice is adjusted to minimize the variation of the time of flight with respect to energy (which is what allows the use of constant-frequency RF).

The EMMA experiment will not simply demonstrate that one can accelerate a beam in a linear non-scaling FFAG. The machine will be used to study single-particle beam dynamics in such a system. While we may not have a precise match between the dynamics predicted by simulation and the behavior of the machine, due to imperfect modeling of magnets as well as errors in the machine, we should still be able to verify that the dependency of measurable quantities in the machine on machine parameters (magnet excitations and positions, RF voltages and frequencies, etc.) are correct.

There are several effects that appear in linear non-scaling FFAGs, in particular for the configuration used for muon acceleration, that are known to be of significance. The first is the accelerating mode itself, often referred to as "serpentine" acceleration, that appears in linear non-scaling FFAGs that use high-frequency RF and are isochronous within their energy range [13–17]. This mode of acceleration is has never been used in an accelerator before. When it is used to accelerate rapidly, it is linac-like, but it is more interesting when it is used to accelerate as slowly as possible. The EMMA experiment will therefore try to probe the parameter space of this accelerating mode, to verify that it behaves as expected. In particular, this requires that one be able to change the time of flight as a function of energy, while making minimal changes to the tunes as a function of energy. As a result, the machine must be able to vary the dipole and quadrupole components of the lattice independently. We chose to do this by constructing quadrupole magnets and putting them on sliders that allowed them to be moved horizontally. In addition to varying the time of flight, we will vary the RF voltage in the lattice as well to further explore the parameter space for serpentine acceleration.

The second effect of interest is resonances (though "resonance" may not be precisely the right term [18]). Because the machine tune varies with energy, one expects to cross a number of resonances. A linear non-scaling FFAG is designed to minimize the effect of these resonances by minimizing the driving terms for the resonances and by crossing any resonances rapidly. The driving of the resonances

Email address: jsberg@bnl.gov (J. Scott Berg).
URL: http://pubweb.bnl.gov/people/jsberg/ (J. Scott Berg).
[1] Work Supported by the United States Department of Energy, Contract No. DE-AC02-98CH10886.

is minimized by constructing a lattice consisting entirely of identical, compact cells, and by using linear magnets which should reduce the driving of nonlinear magnets. Any breaking of the perfect symmetry can lead to emittance growth and orbit distortion [18]. In addition, some authors have found significant effects due to nonlinearities when realistic magnets are used in a linear non-scaling FFAG [19,4,18]. To study imperfections, we plan to vary the position and gradient in some individual magnets. For the study of nonlinear resonance effects, we will vary the tune of the lattice to change which nonlinear resonances we cross during the acceleration cycle.

2. Mathematical Description

The computations here are based on a code which symplectically integrates Hamiltonian equations of motion. The code also has a method for estimating the effects of magnet end fields by using a lumped approximation known as a "hard-edge" approximation. Furthermore, the code carefully treats coordinate system translations and rotations. This section gives a mathematical description of the algorithms used in the code.

2.1. *Hamiltonian*

I will use a rectilinear coordinate system to describe the motion. The coordinates are x, y, and s, the latter being the independent variable in the equations of motion. x is in the horizontal direction, and y is in the vertical direction. There is a third coordinate variable, the arrival time t. The three coordinates x, y, and t have conjugate momenta p_x, p_y, and $-E$ respectively.

The motion is governed by the Hamiltonian

$$H = -qA_s - \sqrt{(E/c)^2 - (p_x - qA_x)^2 - (p_y - qA_y)^2}, \quad (1)$$

where A_x, A_y, and A_s are the components of the magnetic vector potential in the x, y, and s directions respectively. Hamilton's equations of motion are

$$\begin{aligned} \frac{dx}{ds} &= \frac{\partial H}{\partial p_x} \quad \frac{dy}{ds} = \frac{\partial H}{\partial p_y} \quad \frac{dt}{ds} = -\frac{\partial H}{\partial E} \\ \frac{dp_x}{ds} &= -\frac{\partial H}{\partial x} \quad \frac{dp_y}{ds} = -\frac{\partial H}{\partial y} \quad \frac{dE}{ds} = \frac{\partial H}{\partial t}. \end{aligned} \quad (2)$$

2.2. *Quadrupole Field*

The magnet will be described using a so-called "hard-edge" model. In this model, the magnet consists of an entrance edge, the magnet body, and an exit edge. The handling of the entrance and exit edges will be described in a subsequent section. If the magnet has a gradient B_1 and extends from longitudinal positions s_0 to s_1, the field in the body is described by the vector potential

$$A_s = -\frac{B_1}{2} H(s - s_0) H(s_1 - s)(x^2 - y^2), \quad (3)$$

where

$$H(s) = \begin{cases} 1 & s > 0 \\ 1/2 & s = 0 \\ 0 & s < 0 \end{cases} \quad (4)$$

Note the distinction between the function $H(s)$ and the Hamiltonian H: the function will always have an argument in parentheses. The vector potential components A_x and A_y are 0.

2.3. *Integration Algorithm*

The equations of motion (2) are integrated using the implicit midpoint method which is turned into a fourth order integrator using Yoshida's algorithm [20]. This results in a symplectic integrator. For the purposes of defining the EMMA lattice, this discussion is merely academic: the equations of motion are integrated to high accuracy, and the results are thus independent of the integration method.

The implicit midpoint performs a step of size Δs for a vector field $\boldsymbol{v}(\boldsymbol{z}, s)$ by solving the implicit equations

$$\boldsymbol{z}_\mathrm{f} = \boldsymbol{z}_\mathrm{i} + \Delta s\, \boldsymbol{v}\big((\boldsymbol{z}_\mathrm{i} + \boldsymbol{z}_\mathrm{f})/2, s + \Delta s/2\big), \quad (5)$$

where $\boldsymbol{z}_\mathrm{i}$ are the initial phase space variables, and $\boldsymbol{z}_\mathrm{f}$ are the phase space variables at the end of the step. If $\boldsymbol{v}$ is derived from a Hamiltonian, for which case

$$v_i = \sum_j J_{ij} \frac{\partial H}{\partial z_j}, \quad (6)$$

where $J_{xp_x} = J_{yp_y} = J_{Et} = 1$, $J_{p_x x} = J_{p_y y} = J_{tE} = -1$, and $J_{ij} = 0$ otherwise, the algorithm is symplectic. The algorithm is accurate to second order in Δs. This algorithm is particularly convenient for cases that have a transverse vector potential. Its disadvantage is that it is iterative, typically requiring around 6 evaluations of the vector field $\boldsymbol{v}$ and its derivative.

The implicit equation is solved using Newton's method. Application of Newton's method requires the derivative A of the vector field, which is

$$A_{ij} = \sum_k J_{ik} \frac{\partial^2 H}{\partial z_k \partial z_j}. \quad (7)$$

Newton's method then gives

$$\boldsymbol{z}_{\mathrm{f},n+1} = \boldsymbol{z}_{i,n} + (I - \Delta s A/2)^{-1} \boldsymbol{\delta}_n, \quad (8)$$

where

$$\boldsymbol{\delta}_n = \boldsymbol{z}_\mathrm{i} + \Delta s\, \boldsymbol{v}\big((\boldsymbol{z}_\mathrm{i} + \boldsymbol{z}_\mathrm{f})/2, s + \Delta s/2\big) - \boldsymbol{z}_\mathrm{f}. \quad (9)$$

Note that A is evaluated at $(\boldsymbol{z}_\mathrm{i} + \boldsymbol{z}_\mathrm{f})/2$ just as $\boldsymbol{v}$ is.

For the algorithm to be symplectic, the iteration must converge to machine precision. The algorithm determines that is has reached machine by keeping track of a boolean bounce vector $\boldsymbol{b}$. Initially every element of $\boldsymbol{b}$ is set to false. After an iteration n of Newton's method, the difference $\boldsymbol{\delta}_n$ is computed. If $\delta_{ni} = 0$, or if $|\delta_{ni}| \geqslant |\delta_{nf}|$, then b_i is set to true. The iteration terminates once every component of $\boldsymbol{b}$

is true (note that a component of $\boldsymbol{b}$ may have become true at the latest iteration or any prior one).

One can also obtain the derivative map about the orbit that one finds by this algorithm. It is readily available since the derivative of the vector field is needed for Newton's method anyhow. If $\boldsymbol{z}_0(s)$ is a solution to the equations of motion, then to lowest order in $\boldsymbol{z} - \boldsymbol{z}_0$, the solution $\boldsymbol{z}$ near $\boldsymbol{z}_0$ is given by

$$\boldsymbol{z}(s) = \boldsymbol{z}_0(s) + M(s; s_0)[\boldsymbol{z}(s_0) - \boldsymbol{z}_0(s_0)]. \tag{10}$$

The evolution of M from one step to the next is given by

$$M_\mathrm{f} = (I - \Delta s A/2)^{-1}(I + \Delta s A/2)M_\mathrm{i}. \tag{11}$$

Note that no additional iteration is needed to obtain M; iteration is only necessary for finding $\boldsymbol{z}_\mathrm{f}$.

Instead of Newton's method, one could use fixed-point iteration to obtain the solution:

$$\boldsymbol{z}_{\mathrm{f},n+1} = \boldsymbol{z}_\mathrm{i} + \Delta s\, \boldsymbol{v}\big((\boldsymbol{z}_\mathrm{i} + \boldsymbol{z}_{\mathrm{f},n})/2, s + \Delta s/2\big). \tag{12}$$

One can always choose Δs small enough so that the algorithm does converge. while this avoids the computation of A, it takes more steps to converge; the net result is that there is little difference in the time taken for the fixed point iteration and Newton's method; I chose to use Newton's method since it converges over a broader range of step sizes.

Viewing the implicit midpoint method as a mapping on a phase space vector which depends on the step size Δs, I will write it as the map $\mathcal{S}_2(\Delta s)$. Since $\mathcal{S}_2(-\Delta s) = \mathcal{S}_2^{-1}(\Delta s)$, it satisfies the conditions required for Yoshida's method [20] to construct higher order integrators. Thus, in particular, a fourth order integrator with step size s is constructed as

$$\mathcal{S}_4(\Delta s) = \mathcal{S}_2(a_1\Delta s)\mathcal{S}_2(a_2\Delta s)\mathcal{S}_2(a_1\Delta s) \tag{13}$$

$$a_1 = \sqrt[3]{4}(\sqrt[3]{2}+1)^2/6 \quad a_2 = -(\sqrt[3]{2}+1)^2/3. \tag{14}$$

Thus, the implicit midpoint method is applied three times, with Δs replaced by $a_1\Delta s$, $a_2\Delta s$, and $a_1\Delta s$ in sequence, to obtain a fourth order integrator.

2.4. *Step Size*

The algorithm uses a fixed step size Δs, in the examples here it is 1 mm. However, the length of most elements will not be an exact multiple of 1 mm. For the optimization process, all results should be a continuous function of the length of the elements. In addition, if an element is symmetric with respect to the direction through which one traverses the element, the integration algorithm should preserve that property. To satisfy all of these requirements, the integration steps are chosen as follows: taking L to be the length of the element, define

$$n = \left\lfloor \frac{L - \Delta s}{2\Delta s} \right\rfloor \qquad \epsilon = \frac{L - (2n+1)\Delta s}{2}. \tag{15}$$

The algorithm takes one step of ϵ, $2n+1$ steps of Δs, and one step of ϵ, in that order. One can straightforwardly verify that this stepping algorithm satisfies all the desired properties, and if $L \leqslant \Delta s$, it takes a single step.

2.5. *Magnet Ends*

The effects of the variation of the fields at the ends of the magnet are encapsulated into a single mapping at the entrance and exit of the magnet. Such a mapping can be computed to lowest order in the body field of the magnet and to lowest order in the transverse variables [21,22]. The map, assuming that the quadrupole field maintains its quadrupole symmetry as the field magnitude varies, can be written as a Lie algebraic map $e^{:f:}$ [23,24] with the generator (computed to lowest order in the transverse variables)

$$f = -\Delta B_1 \frac{p_x(x^3 + 3xy^2) - p_y(3x^2y + y^3)}{12}. \tag{16}$$

Since the computation is only correct to first order in the body field, the Lie map need only be evaluated correctly to first order in the generator, but should be evaluated symplectically. One can do this straightforwardly using the implicit midpoint method, which evaluates the map symplectically to second order in the generator. The method is similar to the one used for integration: one iteratively solves

$$\boldsymbol{z}_\mathrm{f} = \boldsymbol{z}_\mathrm{i} - J\boldsymbol{\nabla} f\big((\boldsymbol{z}_\mathrm{f} + \boldsymbol{z}_\mathrm{i})/2\big) \tag{17}$$

for $\boldsymbol{z}_\mathrm{f}$.

As for integration, the local derivative will transform as

$$M_\mathrm{f} = (I + B/2)^{-1}(I - B/2)M_\mathrm{i} \tag{18}$$

where

$$B_{ij} = \sum_k J_{ik}\partial_j\partial_k f\big((\boldsymbol{z}_\mathrm{i} + \boldsymbol{z}_\mathrm{f})/2\big). \tag{19}$$

Note that this transformation can result in a nonzero displacement at the magnet end. This is correct behavior. It corresponds to a particle getting a large transverse momentum kick on entering the end field, moving a short distance in the end field, then receiving the opposite kick. In the limit as the length of the end field goes to zero, the displacement is nonzero.

2.6. *Translations*

Transverse coordinate translations are trivial: for a transverse translation by $(\Delta x, \Delta y)$, one simply transforms as

$$x_\mathrm{f} = x_\mathrm{i} - \Delta x \qquad y_\mathrm{f} = y_\mathrm{i} - \Delta y. \tag{20}$$

Note the negative sign for Δx and Δy: this will depend on what exactly one means by "translation," so one should think carefully about what these signs should be. With the signs shown, the center of the coordinate system moves by the vector $(\Delta x, \Delta y)$.

2.7. *Coordinate Rotation about Vertical Axis*

A coordinate rotation about the vertical axis is not a simple coordinate transformation, since the independent variable s must be involved. The transformation involves two steps: one is transporting the beam to the plane defined by

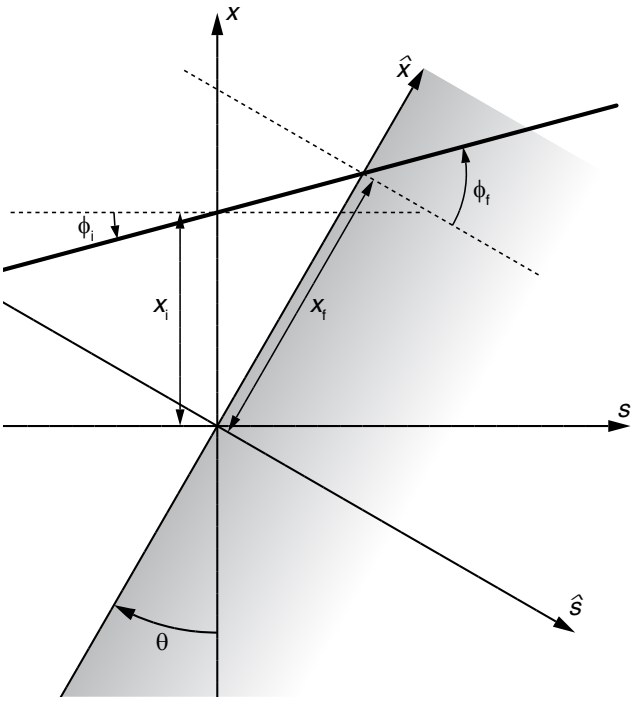

Fig. 1. Coordinate system defining a rotation about the vertical axis, at the entrance to the magnet. The coordinate axes change from (x, s) to $(\hat{x}, \hat{s})$. The shaded area shows where the magnet would be. The thickest line is the beam.

the post-rotation coordinates, the other is the actual rotation. The primary purpose of the rotation in this context is to change into the local coordinate system of a magnet whose axis is not parallel to the current coordinate system.

First, let's examine the transformation at the entrance to the magnet. In the original coordinates, the particle has transverse coordinates $(x_\mathrm{i}, y_\mathrm{i})$ and has corresponding momenta $(p_{x\mathrm{i}}, p_{y\mathrm{i}})$, an initial time t_i and an energy E (which will not change). Figure 1 shows the geometry in the x-s plane. The angle ϕ_i is related to the momenta by

$$\sin\phi_\mathrm{i} = \frac{p_{x\mathrm{i}}}{\sqrt{(E/c)^2 - (mc)^2 - p_{y\mathrm{i}}^2}}. \tag{21}$$

The particle travels in a drift until it enters the magnet; thus all trajectories are straight lines. Planar geometry can then be used to relate x_f and ϕ_f to x_i and ϕ_i:

$$\phi_\mathrm{f} = \phi_\mathrm{i} + \theta \qquad x_\mathrm{f} = \frac{\cos\phi_\mathrm{i}}{\cos(\theta+\phi_\mathrm{i})} x_\mathrm{i}. \tag{22}$$

Converting the angles back into momenta, taking into account the fact that p_y is invariant,

$$x_\mathrm{f} = \frac{p_{s\mathrm{i}} x_\mathrm{i}}{p_{s\mathrm{i}}\cos\theta - p_{x\mathrm{i}}\sin\theta} \tag{23}$$

$$p_{x\mathrm{f}} = p_{x\mathrm{i}}\cos\theta + p_{s\mathrm{i}}\sin\theta \tag{24}$$

where

$$p_{s\mathrm{i}} = \sqrt{(E/c)^2 - (mc)^2 - p_{x\mathrm{i}}^2 - p_{y\mathrm{i}}^2}. \tag{25}$$

The distance traveled in the x-s plane in the drift is

$$\frac{\sin\theta}{\cos(\theta+\phi_\mathrm{i})} x_\mathrm{i} = \frac{x_\mathrm{i}\sin\theta\sqrt{(E/c)^2 - (mc)^2 - p_y^2}}{p_{s\mathrm{i}}\cos\theta - p_{x\mathrm{i}}\sin\theta}. \tag{26}$$

From this, the vertical displacement along that path is

$$y_\mathrm{f} = y_\mathrm{i} + \frac{x_\mathrm{i} p_{y\mathrm{i}}\sin\theta}{p_{s\mathrm{i}}\cos\theta - p_{x\mathrm{i}}\sin\theta}, \tag{27}$$

and the time along that trajectory is

$$t_\mathrm{f} = t_\mathrm{i} + \frac{x_\mathrm{i} E\sin\theta}{c^2[p_{s\mathrm{i}}\cos\theta - p_{x\mathrm{i}}\sin\theta]}. \tag{28}$$

The same set of transformations applies at the magnet exit.

The derivative of the transformation can be found straightforwardly by differentiating the above equations.

3. Lattice Description

The machine was designed to accelerate from 10 to 20 MeV in kinetic energy. A factor of 2 in energy is typical and probably optimal for muon acceleration. Anything significantly less would be a rather unimpressive amount of acceleration for a ring. Lowering the energy would reduce the performance of the machine significantly [25,26]. Increasing the energy would require a longer lattice and either more cells and higher fields or a reduced performance.

When operating in a rapid-accelerating mode, a linear non-scaling FFAG should have a large dynamic aperture due to its linear magnets and the fact that it accelerates through resonances rapidly. The EMMA lattice is designed so that in all operating configurations, it has a normalized transverse acceptance of 3 mm. If a is the maximum beam deviation from the energy-dependent closed orbit and the motion is perfectly linear, the transverse normalized acceptance is $a^2 p/(mc\beta)$, where p is the momentum of the closed orbit in question, β is the Courant-Snyder beta function on that orbit, m is the particle mass, and c is the speed of light. The quantity of 3 mm comes from scaling the muon acceleration lattices, which are designed to have a normalized transverse acceptance of 30 mm. For reaching to a comparable level of dynamic aperture, the lattice angles and fractional occupation of the magnet aperture should be comparable. The result is that for similar numbers of cells and ratios of momentum to rest mass, the acceptance should scale with the cell length. In addition to exploring the dynamic aperture of the machine, we wish also to have sufficient transverse acceptance to explore the dependence of time-of-flight on transverse amplitude, which is an important effect in linear non-scaling FFAGs which accelerate beams with large transverse emittance [27–30].

The product of the number of cells and the number of turns achievable with an a value (see [17]) of 1/12 (an estimate of a minimal value for a which gives a reasonably-sized longitudinal phase space acceptance) was used to characterize the performance of the design. A higher value for this quantity reduces the discretization in the acceleration process (which is an important effect [18]) and reduces the rate of resonance crossing (which we would like to be small

so that the effect can be studied). Since muon accelerators typically have that value in the range of 500–1500, and since the size of the ring increases with that number, 500 was chosen for the goal for that quantity.

For the RF frequency, 1.3 GHz and 2.856 GHz were considered, since they are compact and power is readily available at these frequencies. The 2.856 GHz lattices required significantly more lattice cells than the 1.3 GHz lattices, and thus 1.3 GHz was chosen.

The lattice consists of a combined-function doublet cell, repeated 42 times. Doublet cells generally give most cost-effective lattice configuration for a linear non-scaling FFAG [25], though there are exceptions. The choice of 42 cells was motivated by several considerations. First, one has the desire to achieve 500 cell-turns. A multiple of 6 cells was considered helpful from the point of view of reducing the driving of resonance terms, and in any case is a reasonable level of discretization. The number of cells required is reduced slightly as the pole tip fields are increased, but levels off once the magnet pole tip fields get very high, since the cell length becomes dominated by elements other than magnets. Thus, it becomes impractical to reduce the number of cells to 36, and therefore 42 is the minimum multiple of 6.

From an engineering point of view, it is convenient to lay the cavity and two magnets in a single cell out with their axes aligned. The penalty for doing so instead of aligning the magnets and cavities separately was an aperture increase of less then 1 mm. Thus, the ring is described in a coordinate system based on a 42-sided polygon. The corners of the polygon are just at the ends of the D magnets adjacent to the drifts which hold cavities, since the D magnet is where most of the bending occurs, and one wants the magnet axes within the doublet itself aligned (as opposed to the magnet axes on opposite sides of the cavity drift). The long drift which can hold a cavity was chosen to be 21 cm long to give sufficient space for the cavity, and the drift between the (idealized) quadrupoles was chosen to be 5 cm.

Once these lattice parameters were chosen, eight lattice configurations were chosen based on their tunes and on the behavior of the time of flight as a function of energy. To be precise, tunes and times of flight as a function of energy are computed by first finding the closed orbit and a linear matrix for motion about the closed orbit at the energy in question. The time of flight is then the time a particle needs to follow the closed orbit, and the tunes are derived from the eigenvalues of the matrix about the closed orbit.

3.1. *The Baseline Lattice (070221b)*

The baseline lattice will be used to set the magnet lengths, which will remain fixed for subsequent lattice configurations. It was chosen to have a relatively high horizontal tune, which reduces the time of flight variation with energy and therefore increases increases the number of turns over which one can accelerate [31], and to avoid the $\nu_x - 2\nu_y = 0$ resonance line, which was found to give significant nonlinear coupling between the transverse planes in some circumstances [18].

Table 1
Lattice parameters common to all configurations.

Cells	42
RF frequency	1.3 GHz
Harmonic number	72
Long drift length	210.000 mm
F quad length	58.782 mm
Short drift length	50.000 mm
D quad length	75.699 mm

In the design of this lattice, there are 6 parameters that can be varied: two magnet lengths, two quadrupole strengths, and two quadrupole displacements. The lattice will meet the following constraints:

(i) The time of flight is identical at the low and high energy.
(ii) The 15 MeV kinetic energy closed orbit crosses the line segment that defines the coordinate system at the center of the long drift.
(iii) The following three distances in the single-cell tune plane are equal (giving two constraints):
  (a) The distance from the low-energy tune to the $\nu_x - \nu_y = 0$ resonance line, with the low-energy tune on the high-ν_x/low-ν_y side of the line.
  (b) The distance from the low-energy tune to the $\nu_x + 2\nu_y = 1$ resonance line, with the low-energy tune on the high-ν_x/high-ν_y side of the line.
  (c) The distance from the high-energy tune to the $\nu_x - 2\nu_y = 0$ resonance line, with the high-energy tune on the low-ν_x/high-ν_y side of the line.
(iv) 0.75 times the minimum time of flight plus 0.25 times the maximum time of flight, all multiplied by 42, is 72 times the period of 1.3 GHz RF.
(v) The maximum fields on a circle that encloses the 3 mm normalized acceptance linear ellipses (i.e., motion is assumed to be linear about the closed orbit for this purpose) for all energies is the same for both quadrupoles. See [32] for a method for computing this.

There are six parameters and six constraints, so if there is a solution, it should be locally unique. The resulting quadrupole lengths are given in Tab. 1 and the required magnet displacements, quadrupole gradients, magnet and vacuum chamber apertures, and RF frequency range are given in Tab. 2. The range in RF frequencies is defined so that any energy within the 10–20 MeV energy range of the machine can be synchronized with the RF. This is not only used for varying the parameters for the longitudinal dynamics (the b parameter in [17]), but is also potentially useful during commissioning to keep the beam energy fixed even in the presence of losses from beam loading or other wakefield losses.

In reality, there is a slight inaccuracy in this description:

Table 2
Lattice parameters for individual configurations. The maximum and minimum positions are for a rectangle which encompasses all of the 3 mm normalized beam ellipses for all energies. Coordinates are defined relative to the position of the coordinate system defined in the text. In addition, rectangles are given relative to the quadrupole center.

	070221b	070221c	070221d	070221e	070221f	070221g	070221h	070221i
D displacement (mm)	34.048	39.195	46.532	40.797	28.751	39.491	37.142	48.559
F displacement (mm)	7.514	8.171	9.535	7.684	4.903	10.030	6.329	10.212
D gradient (T/m)	-4.704	-4.126	-3.597	-3.764	-4.843	-4.551	-3.832	-3.593
F gradient (T/m)	6.695	6.108	5.230	6.553	6.847	6.526	6.642	6.346
Minimum coordinate in D (mm)	-4.280	-4.836	-7.416	-3.875	-5.690	-3.069	-4.409	-3.109
Maximum coordinate in D (mm)	17.620	17.966	18.789	17.215	17.620	17.435	17.391	16.619
Minimum quad coordinate, D (mm)	-38.328	-44.031	-53.948	-44.672	-34.441	-42.560	-41.551	-51.661
Maximum quad coordinate, D (mm)	-16.428	-21.228	-27.743	-23.581	-11.130	-22.056	-19.750	-31.939
Half height, D (mm)	10.987	10.129	9.764	11.668	11.015	10.961	11.664	11.676
Minimum coordinate in F (mm)	-19.000	-18.806	-21.638	-17.434	-19.347	-18.815	-17.250	-17.999
Maximum coordinate in F (mm)	19.509	19.345	19.509	18.660	20.700	18.185	19.509	16.783
Minimum quad coordinate, F (mm)	-26.514	-26.977	-31.173	-25.117	-24.250	-28.845	-23.579	-28.212
Maximum quad coordinate, F (mm)	11.995	11.174	9.974	10.977	15.797	8.155	13.180	6.571
Half height, F (mm)	5.596	6.183	6.511	8.897	5.544	5.633	8.895	8.906
Minimum coordinate in cavity (mm)	-13.680	-14.031	-16.936	-12.491	-14.431	-13.089	-12.588	-12.515
Maximum coordinate in cavity (mm)	17.026	17.026	17.408	16.247	17.814	16.048	16.882	-14.708
Half height, cavity (mm)	7.806	7.453	7.499	10.554	7.875	7.731	10.571	10.513
Minimum frequency deviation (kHz)	-2198	-2311	-2571	-2100	-2244	-3930	-2183	-4019
Maximum frequency deviation (kHz)	723	882	1367	457	1554	-4	-842	-193

this procedure was followed for an earlier version of the lattice where the magnets and cavity didn't have their axes parallel. At that point the magnet lengths were fixed. The last two constraints above were then removed and the precise parameters for this lattice were computed. If the full procedure here were followed, however, the results should be almost identical.

3.2. *The Medium Tune Lattice (070221c)*

This lattice is similar to the baseline lattice, except that it will not cross the $\nu_x + 2\nu_y = 1$ resonance. Due to the lower horizontal tunes, this lattice will have a larger time of flight range than the baseline lattice, and will therefore not allow for as many turns of acceleration.

The lengths from the baseline lattice are adopted for this lattice and all subsequent lattices. We will vary the quadrupole strengths and displacements, giving 4 variable parameters (similarly in all subsequent lattices). The lattice will meet the following constraints:

(i) The time of flight is identical at the low and high energy.

(ii) The following three distances in the single-cell tune plane are equal (giving two constraints):
  (a) The distance from the low-energy tune to the $3\nu_x = 1$ resonance line, with the low-energy tune on the high-ν_x side of the line.
  (b) The distance from the low-energy tune to the $\nu_x + 2\nu_y = 1$ resonance line, with the low-energy tune on the low-ν_x/low-ν_y side of the line.
  (c) The distance from the high-energy tune to the $\nu_x - 2\nu_y = 0$ resonance line, with the high-energy tune on the low-ν_x/high-ν_y side of the line.

(iii) The increase in the horizontal pipe size in the magnets and cavity from the baseline is minimized. To compute this, the maximum and minimum coordinates of a 3 mm normalized acceptance linear ellipse about the energy-dependent closed orbit over the entire length of each element and over all energies is computed (6 quantities, two for each element). If the quantity in question is larger, in the case of a maximum, or smaller, in the case of a minimum, than the corresponding quantity in the baseline lattice, the difference (always a positive number) is added to a sum. If the sum is zero (because the beam is always inside the beam pipe from the baseline), then instead, one computes the amounts by which a maximum was less than the corresponding maximum for the baseline or a minimum was greater than the corresponding minimum for the baseline, chooses the smallest of these 6 numbers, takes its negative, and replaces the sum with that. This "sum" is the quantity that is minimized.

The required magnet displacements, quadrupole gradients,

magnet and vacuum chamber apertures, and RF frequency range are given in Tab. 2 (and for all subsequent lattice configurations).

3.3. *The Low Tune Lattice (070221d)*

This lattice is similar to the medium tune lattice, except that it will not cross the $3\nu_x = 1$ resonance. This lattice will have an even larger time of flight range than the medium tune lattice, and its beam size will generally define the pipe, cavity, and magnet apertures.

The lattice will meet the following constraints:

(i) The time of flight is identical at the low and high energy.

(ii) The following three distances in the single-cell tune plane are equal (giving two constraints):
  (a) The distance from the low-energy tune to the $\nu_x - \nu_y = 0$ resonance line, with the low-energy tune on the high-ν_x/low-ν_y side of the line.
  (b) The distance from the low-energy tune to the $3\nu_x = 1$ resonance line, with the low-energy tune on the low-ν_x side of the line.
  (c) The distance from the high-energy tune to the $\nu_x - 2\nu_y = 0$ resonance line, with the high-energy tune on the low-ν_x/high-ν_y side of the line.

(iii) The increase in the horizontal pipe size in the magnets and cavity from the baseline is minimized, as described in the previous subsection.

3.4. *The High Efficiency Lattice (070221e)*

This lattice is at attempt to imitate the design of a optimal performing muon acceleration lattice, in the sense that it maximizes the number of turns in the machine (by reducing the time of flight range) and minimizes the required magnet fields. It accomplishes this by making the horizontal tune as high as practical and the vertical tune as low as is practical.

The lattice thus meets the following constraints:

(i) The time of flight is identical at the low and high energy.

(ii) The low-energy horizontal tune is 0.4.

(iii) The high-energy vertical tune is 0.05.

(iv) The increase in the horizontal pipe size in the magnets and cavity from the baseline is minimized.

3.5. *The Baseline Lattice, with Minimum Time at Lower Energy (070221f)*

This lattice, as well as the next three, allow for the study of the dependence of the longitudinal dynamics on the energy of the minimum in the time of flight as a function of energy. This lattice meets the same tune constraints as the baseline lattice, but moves that minimum to approximately the lowest energy that we can without unduly increasing the aperture requirement.

The lattice meets the following constraints:

(i) The minimum time of flight is at 14 MeV kinetic energy.

(ii) The following three distances in the single-cell tune plane are equal (giving two constraints):
  (a) The distance from the low-energy tune to the $\nu_x - \nu_y = 0$ resonance line, with the low-energy tune on the high-ν_x/low-ν_y side of the line.
  (b) The distance from the low-energy tune to the $\nu_x + 2\nu_y = 1$ resonance line, with the low-energy tune on the high-ν_x/high-ν_y side of the line.
  (c) The distance from the high-energy tune to the $\nu_x - 2\nu_y = 0$ resonance line, with the high-energy tune on the low-ν_x/high-ν_y side of the line.

(iii) The increase in the horizontal pipe size in the magnets and cavity from the baseline is minimized.

3.6. *The Baseline Lattice, with Minimum Time at Higher Energy (070221g)*

This lattice is like the previous lattice, but instead the minimum in the time of flight is shifted to approximately the highest energy possible without unduly increasing the aperture requirement.

The lattice meets the following constraints:

(i) The minimum time of flight is at 15.5 MeV kinetic energy.

(ii) The following three distances in the single-cell tune plane are equal (giving two constraints):
  (a) The distance from the low-energy tune to the $\nu_x - \nu_y = 0$ resonance line, with the low-energy tune on the high-ν_x/low-ν_y side of the line.
  (b) The distance from the low-energy tune to the $\nu_x + 2\nu_y = 1$ resonance line, with the low-energy tune on the high-ν_x/high-ν_y side of the line.
  (c) The distance from the high-energy tune to the $\nu_x - 2\nu_y = 0$ resonance line, with the high-energy tune on the low-ν_x/high-ν_y side of the line.

(iii) The increase in the horizontal pipe size in the magnets and cavity from the baseline is minimized.

3.7. *The High Efficiency Lattice, with Minimum Time at Lower Energy (070221h)*

This lattice is like that of Sec. 3.5, except that the tune range matches that of the high efficiency lattice.

The lattice meets the following constraints:

(i) The minimum time of flight is at 14 MeV kinetic energy.

(ii) The low-energy horizontal tune is 0.4.

(iii) The high-energy vertical tune is 0.05.

(iv) The increase in the horizontal pipe size in the magnets and cavity from the baseline is minimized.

Table 3
Summary of parameters related to the magnets. Note that the maximum pipe size does not occur for the largest magnet displacement, so the pipe will penetrate further into the magnet aperture than the beam ever will.

	D	F
Minimum shift (mm)	28.751	4.903
Maximum shift (mm)	48.559	10.212
Maximum gradient (T/m)	-4.843	6.847
Minimum pipe horizontal (mm)	-7.416	-21.638
Maximum pipe horizontal (mm)	18.789	20.700
Maximum half height (mm)	11.676	8.906
Maximum pipe horizontal in quad (mm)	-55.975	-31.850
Maximum beam horizontal in quad (mm)	-53.948	-31.173

Table 4
Summary of parameters related to the cavity.

Minimum pipe horizontal	-16.936 mm
Maximum pipe horizontal	17.814 mm
Maximum half height	10.571 mm
Cavity center position	0.439 mm
Cavity aperture diameter	34.751 mm
Minimum frequency deviation	-4019 kHz
Maximum frequency deviation	1554 kHz

3.8. *The High Efficiency Lattice, with Minimum Time at Higher Energy (070221i)*

This lattice is like that of Sec. 3.6, except that the tune range matches that of the high efficiency lattice.

The lattice meets the following constraints:

(i) The minimum time of flight is at 15.5 MeV kinetic energy.
(ii) The low-energy horizontal tune is 0.4.
(iii) The high-energy vertical tune is 0.05.
(iv) The increase in the horizontal pipe size in the magnets and cavity from the baseline is minimized.

3.9. *Summary of Lattice Parameters*

From the parameters for all of these lattices, one can construct the minimum dimensions of a rectangular pipe that will enclose all of the beam ellipses. One can determine the maximum distance which this pipe will penetrate into the magnet aperture. One can also determine minimum dimensions for a cavity aperture. All of these parameters and some more are summarized in Tabs. 3 and 4.

Figures 2–5 show the tune and time of flight for a single cell of these lattices.

4. Acknowledgments

The general choice of the EMMA lattice parameters involved the input of a number of individuals. An overall pic-

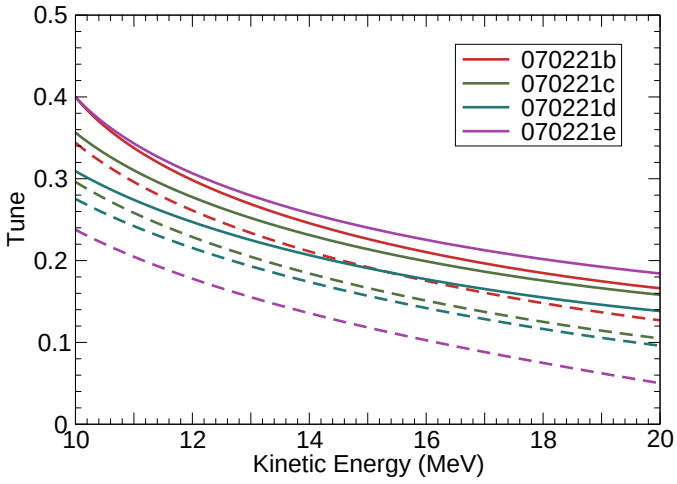

Fig. 2. Tune for a single cell as a function of kinetic energy for four of the lattices. Solid lines are horizontal tunes, dashed lines are vertical. Lattices are color coded. The tunes for the lattices 070221f, 070221g, 070221h, and 070221i are nearly identical to the tunes for the lattices from which they are derived (either 070221b or 070221e; see Fig. 3).

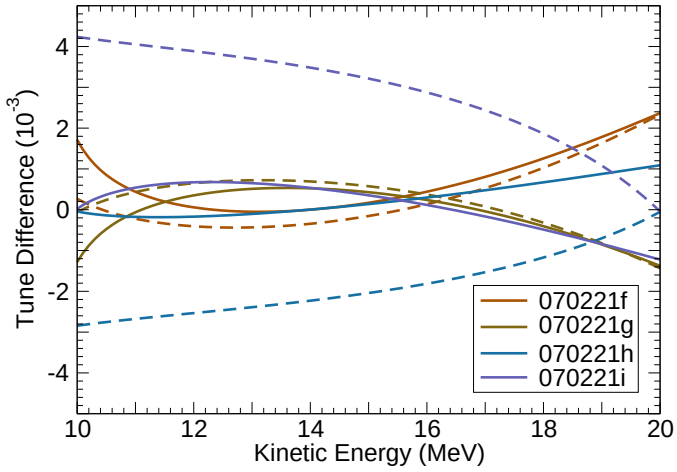

Fig. 3. Difference between the lattice tune and the tune for the lattice from which it was derived (either 070221b or 070221e).

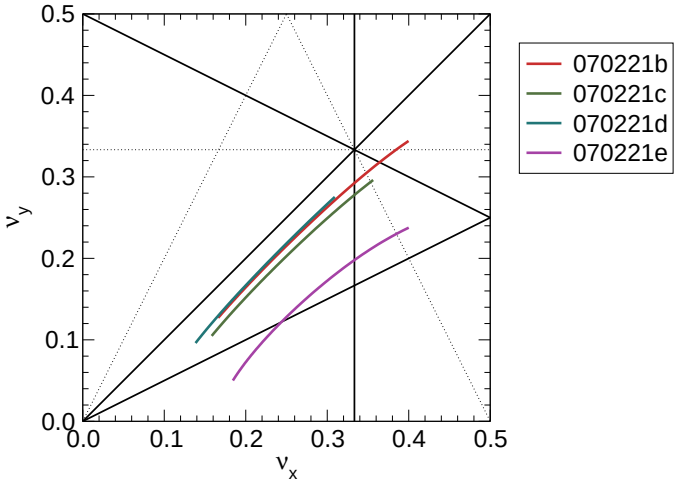

Fig. 4. Tunes from Fig. 2 plotted in the tune plane. Straight lines are resonances through third order for a single cell. Dotted lines are driven by skew terms.

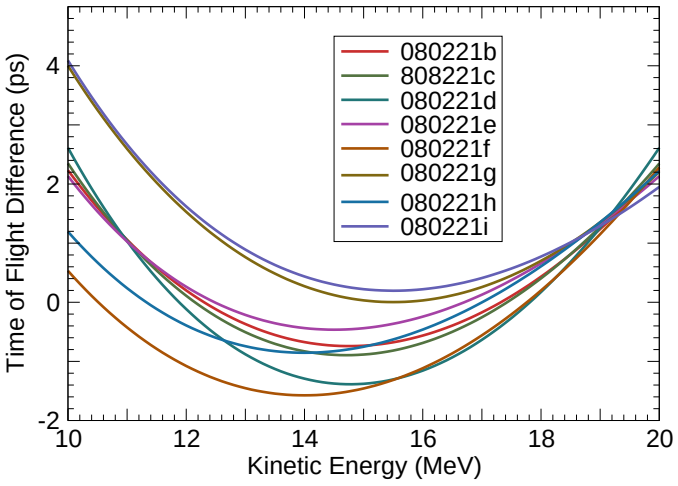

Fig. 5. Time of flight for a single cell as a function of kinetic energy, relative to a time that is synchronized with 1.3 GHz RF at harmonic number 72.

ture of the machine arose from discussions at the FFAG workshop at Brookhaven National Laboratory which occurred October 13–17, 2003 (`http://www.cap.bnl.gov/mumu/conf/ffag-031013/`). At this point we had the approximate size and range of RF frequency for the machine. Subsequent phone meetings at the beginning of 2005 of what is now the EMMA collaboration helped refine these parameters to the point where we had chosen 1.3 GHz RF and 42 doublet cells.

References

[1] C. Johnstone, S. Koscielniak, Recent progress on FFAGs for rapid acceleration, in: Graf [33], p. T508, eConf C010630, SLAC-R-599.
URL `http://www.slac.stanford.edu/econf/C010630/`

[2] C. Johnstone, S. Koscielniak, FFAGs for rapid acceleration, Nucl. Instrum. Methods A 503 (2003) 445–457.

[3] J. S. Berg, FFAGs for muon acceleration, in: W. Chou, J. M. Jowett (Eds.), ICFA Beam Dynamics Newsletter No. 29, ICFA, 2003, pp. 27–33.

[4] J. S. Berg, S. A. Bogacz, S. Caspi, J. Cobb, R. C. Fernow, J. C. Gallardo, S. Kahn, H. Kirk, D. Neuffer, R. Palmer, K. Paul, H. Witte, M. Zisman, Cost-effective design for a neutrino factory, Phys. Rev. ST Accel. Beams 9 (2006) 011001.

[5] A. G. Ruggiero, FFAG accelerator proton driver for neutrino factory, Nucl. Phys. B (Proc. Suppl.) 155 (2006) 315–317.

[6] E. Keil, A. Sessler, D. Trbojevic, Hadron cancer therapy complex employing non-scaling FFAG accelerator and fixed field gantry design, in: Y. Mori, K. Okabe, T. Uesugi (Eds.), The International Workshop on FFAG Accelerators, November 6–10, 2006, KURRI, Osaka, Japan, 2007, pp. 45–53.
URL `http://hadron.kek.jp/FFAG/FFAG06_HP/`

[7] D. Trbojevic, A. G. Ruggiero, E. Keil, N. Neskovic, A. Sessler, Design of a non-scaling FFAG accelerator for proton therapy, in: A. Goto (Ed.), Proceedings of the Seventh International Conference on Cyclotrons and their Applications 2004, Particle Accelerator Society of Japan, 2005, pp. 246–248.

[8] E. Keil, D. Trbojevic, A. M. Sessler, Fixed field alternating gradient accelerators (FFAG) for hadron cancer therapy, in: C. Horak (Ed.), Proceedings of 2005 Particle Accelerator Conference, Knoxville, Tennessee, IEEE, Piscataway, NJ, 2005, pp. 1667–1669.

[9] E. Keil, A. M. Sessler, D. Trbojevic, Hadron cancer therapy complex employing non-scaling FFAG accelerator and fixed field gantry design, in: Proceedings of EPAC 2006, Edinburgh, Scotland, 2006, pp. 1681–1683.

[10] K. Peach, J. Cobb, T. Yokoi, I. Gardner, R. Edgecock, M. Poole, J. Pozimski, B. Cywinski, B. Jones, G. McKenna, B. Vojnovic, K. Kirkby, R. Webb, R. Barlow, A. Elliott, PAMELA—a model for an FFAG based hadron therapy machine, in: Petit-Jean-Genaz [37], pp. 2880–2882.

[11] D. Trbojevic, M. Blaskiewicz, E. D. Courant, A. Ruggiero, J. Kewisch, T. Roser, N. Tsoupas, Electron acceleration for E-RHIC with non-scaling FFAG, in: Proceedings of EPAC 2004, Lucerne, Switzerland [35], pp. 932–934.

[12] A. G. Ruggiero, J. A. anad E. Beebe, A. Pikin, T. Roser, D. Trbojevic, Heavy ion driver with non-scaling FFAG, in: Petit-Jean-Genaz [37], pp. 1880–1882.

[13] J. S. Berg, Longitudinal reference particle motion in nearly isochronous FFAG recirculating accelerators, in: Graf [33], p. T503, eConf C010630, SLAC-R-599.
URL `http://www.slac.stanford.edu/econf/C010630/`

[14] J. S. Berg, Dynamics in imperfectly-isochronous FFAG accelerators, in: Proceedings of EPAC 2002, Paris, France, EPAC, European Physical Society Interdivisional Group on Accelerators, CERN, 2002, pp. 1124–1126.

[15] S. Koscielniak, C. Johnstone, Longitudinal dynamics in an FFAG accelerator under conditions of rapid acceleration and fixed, high rf, in: Chew et al. [34], pp. 1831–1833.

[16] S. Koscielniak, C. Johnstone, Mechanisms for nonlinear acceleration in FFAGs with fixed RF, Nucl. Instrum. Methods A 523 (2004) 25–49.

[17] J. S. Berg, Minimizing longitudinal distortion in a nearly isochronous linear nonscaling fixed-field alternating gradient accelerator, Phys. Rev. ST Accel. Beams 9 (3) (2006) 034001.

[18] S. Machida, D. J. Kelliher, Orbit and optics distortion in fixed field alternating gradient muon accelerators, Phys. Rev. ST Accel. Beams 10 (2007) 114001.

[19] B. Palmer, Study IIa FFAG simulations, Presentation at the FFAG Workshop, TRIUMF, Vancouver, BC, Canada, 15–21 April, 2004 (April 2004).
URL `http://www.triumf.ca/ffag2004/`

[20] H. Yoshida, Construction of higher order symplectic integrators, Phys. Lett. A 150 (1990) 262–268.

[21] J. S. Berg, Higher order hard edge end field effects, in: Proceedings of EPAC 2004, Lucerne, Switzerland [35], pp. 2236–2238.

[22] É. Forest, J. Milutinović, Leading order hard edge fringe fields effects exact in $(1+\delta)$ and consistent with maxwell's equations for rectilinear magnets, Nucl. Instrum. Methods A269 (1988) 474–482.

[23] A. J. Dragt, J. M. Finn, Lie series and invariant functions for analytic symplectic maps, J. Math. Phys. 17 (12) (1976) 2215–2227.

[24] A. J. Dragt, E. Forest, Computation of nonlinear behavior of hamiltonian systems using lie algebraic methods, J. Math. Phys. 24 (12) (1983) 2734–2744.

[25] J. S. Berg, R. B. Palmer, Cost optimization of non-scaling FFAG lattices for muon acceleration, in: Proceedings of EPAC 2004, Lucerne, Switzerland [35], pp. 902–904.

[26] J. S. Berg, Recent results from optimization studies of linear non-scaling FFAGs for muon acceleration, in: S. Machida, Y. Mori, T. Yokoi (Eds.), The International Workshop on FFAG Accelerators, October 13–16, 2004, KEK, Tsukuba, Japan, 2005, pp. 1–8.
URL `http://hadron.kek.jp/FFAG/FFAG04\_HP/`

[27] S. Machida, Tracking study of FFAG, in: Mori et al. [36], pp. 65–71.
URL `http://hadron.kek.jp/FFAG/FFAG05\_HP/`

[28] J. S. Berg, Amplitude dependence of time of flight, in: Mori et al. [36], pp. 73–75.
URL http://hadron.kek.jp/FFAG/FFAG05_HP/

[29] S. Machida, Longitudinal emittance blowup in fixed field alternating gradient muon accelerators, Phys. Rev. ST Accel. Beams 9 (2006) 104002.

[30] J. S. Berg, Amplitude dependence of time of flight and its connection to chromaticity, Nucl. Instrum. Methods A 570 (1) (2007) 15–21.

[31] J. S. Berg, C. Johnstone, Design of FFAGs based on a FODO lattice, in: Chew et al. [34], pp. 2216–2218.

[32] J. S. Berg, Finding the circular magnet aperture which encloses an arbitrary number of midplane-centered ellipese, in: Proceedings of EPAC 2004, Lucerne, Switzerland [35], pp. 2855–2857.

[33] N. Graf (Ed.), Proceedings of Snowmass 2001, 2001, eConf C010630, SLAC-R-599.
URL http://www.slac.stanford.edu/econf/C010630/

[34] J. Chew, P. Lucas, S. Webber (Eds.), Proceedings of the 2003 Particle Accelerator Conference, IEEE, Piscataway, NJ, 2003.

[35] EPAC, Proceedings of EPAC 2004, Lucerne, Switzerland, EPAC, European Physical Society Accelerator Group, 2004.

[36] Y. Mori, M. Aiba, K. Okabe (Eds.), The International Workshop on FFAG Accelerators, December 5–9, 2005, KURRI, Osaka, Japan, 2006.
URL http://hadron.kek.jp/FFAG/FFAG05_HP/

[37] C. Petit-Jean-Genaz (Ed.), Proceedings of PAC07, Albuquerque, New Mexico, USA, IEEE, Piscataway, NJ, 2007.